Acta Crystallographica Section B
Structural Science
ISSN 0108-7681

Structures and phase transitions of trigonal $ZrMo_2O_8$ and $HfMo_2O_8$

Simon Allen, Rebecca J. Ward, Matthew R. Hampson, Richard K. B. Gover and John S. O. Evans*

Department of Chemistry, University of Durham, Science Laboratories, South Road, Durham DH1 3LE, UK

Correspondence e-mail: john.evans@dur.ac.uk

Received 6 October 2003
Accepted 30 October 2003

This paper describes the structures, thermal-expansion properties and phase transitions of the trigonal forms of $ZrMo_2O_8$ and $HfMo_2O_8$. Both phases adopt a $P\bar{3}m$ structure at room temperature and show positive thermal expansion. Both phases also undergo a displacive phase transition at high temperature ($ZrMo_2O_8$ at 487 K and $HfMo_2O_8$ at 463 K) to a higher-symmetry structure that has lower thermal expansion. The structure of the high-temperature α'-AMo_2O_8 form (A = Zr and Hf) has been refined from powder diffraction data in space group $P\bar{3}m1$.

1. Introduction

There has been a considerable amount of recent work on the various polymorphs of materials of the general formula AM_2O_8, particularly those with A = Zr or Hf, and M = Mo or W. Many of these compounds are framework phases built from corner-sharing AO_6 octahedra and MO_4 tetrahedra. Much of the interest has been precipitated by the observation of isotropic negative thermal expansion (NTE) in the cubic phases over a wide temperature range (Mary *et al.*, 1996; Evans, 1999). In addition, many of these materials undergo structural changes involving dynamic O-atom disorder at remarkably low temperatures (Evans *et al.*, 2000; Allen & Evans, 2003, 2004) and under relatively modest applied pressures (Evans *et al.*, 1997; Carlson & Krogh Andersen, 2000; Grzechnik *et al.*, 2001; Krogh Andersen & Carlson, 2001; Muthu *et al.*, 2002).

A remarkable number of different polymorphs of $ZrMo_2O_8$ have been reported in the literature. Trigonal α-$ZrMo_2O_8$ (Auray *et al.*, 1986) and monoclinic β-$ZrMo_2O_8$ (Klevtsova *et al.*, 1989) are the thermodynamically stable ambient-pressure polymorphs at high and low temperatures, respectively. The β-to-α transition occurs at $\sim$960 K (Klevtsova *et al.*, 1989), while the reverse reaction requires prolonged heating at 873 K (Auray *et al.*, 1987). The NTE cubic γ-$ZrMo_2O_8$ form is metastable and converts to trigonal α-$ZrMo_2O_8$ at 663 K (Lind *et al.*, 2002). Under the influence of pressure, trigonal α-$ZrMo_2O_8$ reversibly converts to a structurally related monoclinic phase, termed δ-$ZrMo_2O_8$, at $\sim$1.1 GPa, which further transforms to triclinic ϵ-$ZrMo_2O_8$ above 2.0 GPa (Carlson & Krogh Andersen, 2000). Cubic γ-$ZrMo_2O_8$ also undergoes a reversible pressure-induced first-order phase transition at 0.7 GPa, although details of the resulting distorted cubic phase are not known (Lind *et al.*, 2001). Recently, a new low-temperature metastable polymorph, LT-$ZrMo_2O_8$, was prepared *via* a precursor route and its

structure was determined (Allen & Evans, 2003; Allen, Warmingham *et al.*, 2003). The nomenclature of $ZrMo_2O_8$ phases differs from that of ZrW_2O_8 phases, where α-ZrW_2O_8 generally refers to the cubic rather than the trigonal polymorph. Fewer phases have been reported for $HfMo_2O_8$, but again the trigonal α form was reported in the 1960s (Freundlich & Thoret, 1967; Trunov & Kovba, 1967) and details of its powder pattern were published in 1987 (Auray *et al.*, 1987). Correct atomic coordinates of this phase have not been reported, those in the Inorganic Crystal Structure Database being incorrect (Rimsky *et al.*, 1968; Thoret, 1974). The NTE cubic phase and the preparation of the monoclinic β phase at high pressure have also been reported (Lind *et al.*, 2001; Achary *et al.*, 2002, 2003).

To our knowledge, there has been one brief report of the thermal-expansion properties of a trigonal AM_2O_8 phase in the literature to date (Mittal *et al.*, 1999). These authors presented cell-parameter data at ten different temperatures from 80 to 925 K. The data showed a small negative coefficient of expansion for the *a* axis of the material and an unusual temperature dependence of thermal expansion for the *c* axis. In the light of recent work highlighting the importance of structural phase transitions on the thermal-expansion properties of related materials, a more detailed investigation of this behaviour seemed warranted.

In this paper we report X-ray and neutron powder diffraction studies on trigonal $ZrMo_2O_8$ and $HfMo_2O_8$. Room-temperature structures of both materials are presented, and a series of variable-temperature studies from 17 to ~900 K are described. These experiments reveal that both materials undergo a phase transition to a new higher-symmetry trigonal phase (referred to as α'-AM_2O_8) at high temperature. The high-temperature structures are reported and the mechanism of the phase transition is discussed.

2. Experimental

Trigonal $ZrMo_2O_8$ was prepared according to the method described by Samant *et al.* (1993), except that an extended anneal and a slower ramp rate were used. ZrO_2 was prepared by decomposing $ZrOCl_2{\cdot}xH_2O$ (99.9985%, Alfa) at 1173 K for 4 d. A 1:2 molar ratio of ZrO_2 and MoO_3 (99.95%, Alfa) was ground, pressed into 13 mm pellets and heated at 0.85 K min^{-1} to 975 K for 71 h, with three intermittent re-grindings and re-pressings. A white powder resulted. Trigonal $HfMo_2O_8$ was prepared by heating $HfMo_2O_7(OH)_2(H_2O)_2$ in a platinum crucible at 1000 K for 21 h, with re-grinding at room temperature after the first 4 h. Extended annealing was required to give a sharp diffraction pattern.

Neutron diffraction data were collected using the high-resolution powder diffractometer (HRPD) at the ISIS pulsed neutron source of the Rutherford Appleton Laboratory, UK. Room-temperature data for $ZrMo_2O_8$ were collected for a 12 g sample loaded in a 15 mm cylindrical vanadium can. Data for $HfMo_2O_8$ were collected for a 4.7 g sample loaded in an 8 mm can. Variable-temperature data for $ZrMo_2O_8$ were recorded for a 12.5 g sample loaded in an Al slab can in an AS Scientific cryofurnace. Temperature control was achieved by directly heating the slab can walls using a cartridge heater. Data were collected in 5 K steps, from 293 to 647 K, for 5 min (3 μAh) at each temperature. Two minutes were allowed for temperature change/equilibration between measurements. Better quality data for the high-temperature phase were recorded for 165 min at 647 K.

X-ray diffraction data were collected using a Bruker D8 diffractometer equipped with a Cu tube and a Ge(111) incident-beam monochromator giving Cu $K\alpha_1$ (λ = 1.540598 Å) radiation; data were recorded using an M. Braun PSD-50M linear position-sensitive detector. High-quality room-temperature data for Rietveld refinement were collected over a range of 10–120° 2θ, with a step of 0.0144° and a time per step of 6 ($ZrMo_2O_8$) or 7 s ($HfMo_2O_8$). Accurate room-temperature cell parameters were determined by Rietveld refinement of data sets recorded with an Si internal standard (a = 5.4312 Å).

Variable-temperature X-ray data from 17 to 300 K were collected using an Oxford Cryosystems pHeniX cryostat. Samples were prepared by sprinkling finely ground powder on to a vaseline-coated Al plate. In a typical experiment, 30 min data collections were performed, in the range 12–120° 2θ, as the sample was cooled at 13 K h^{-1}. Data were thus collected in ~6.5 K steps. Mean temperatures for each range were extracted from readings taken at 10 s intervals during the measurements. High-temperature experiments were performed on samples mounted on an amorphous silica disk in an Anton Paar HTK 1200 furnace. Data were typically collected over the range 10–110° 2θ, with a step size of 0.0144°, over a 30 min period and using a heating rate of 0.2 K s^{-1} between temperatures. Temperature calibration was checked at high temperatures using an Al_2O_3 internal standard and at low temperatures using an external standard and the positions of the Al reflections of the sample holder (Taylor, 1984; Wang & Reeber, 2000). Phase-transition temperatures derived from X-ray and neutron experiments were within one experimental step (5 K), thus giving us confidence in the temperature calibration. Above 800 K, minor decomposition of $ZrMo_2O_8$ was evidenced by the growth of reflections due to ZrO_2.

Unit-cell parameters and structural coordinates were derived using the Rietveld method within the *TOPAS* suite of programs (Bruker, 2000). Room-temperature coordinates of α-$ZrMo_2O_8$ and α-$HfMo_2O_8$ were determined by combined Rietveld refinement of neutron data from the 168/90/30° detector banks and X-ray diffraction data. For $ZrMo_2O_8$, a total of 131 parameters were initially refined (one scale factor, 16 fractional atomic coordinates and seven isotropic temperature factors for $ZrMo_2O_8$; one scale factor and an overall temperature factor for a minor ZrO_2 impurity; cell parameters of each phase; and additional parameters to describe backgrounds, instrument constants and peak shapes for the four histograms). An absorption correction of the form $\exp(-abs/d^2)$, where *abs* is a refineable parameter, was applied to the 90°, 30° and X-ray data sets to allow for the slightly different absorption inherent in each data collection. The 30° bank data have counting statistics that are consider-

ably poorer than those of other data sets and therefore only make a small contribution to the overall refinement; these data were included to confirm the absence of higher *d*-spacing superstructure reflections. Good agreement with experimental data was achieved, with *wRp* factors of 0.066/0.127/0.063/0.197/0.084 for all/168/90/30°/X-ray data sets. For the final cycles of refinement, an *hkl* dependence to peak widths was introduced using a sixth-order spherical-harmonic function. A size-dependent additional peak broadening was convoluted onto the basic peak shape according to the magnitude of the spherical-harmonic function and the same correction was applied simultaneously to the 168/90°/X-ray data sets, with appropriate scaling. This process led to an improvement in both the visual quality of the fit and the Bragg/profile agreement factors; the *wRp* factors were 0.051/0.105/0.048/0.197/0.080. This improvement is achieved with only nine extra parameters in the model. The magnitude of the correction is such that the sharpest peaks in the 168° data set (*hk*0 reflections) are approximately 20% narrower than the mean. The observed *hkl* dependence of the peak shapes is unsurprising for a layered structure such as this. Minor remaining discrepancies between the observed and calculated patterns are presumably the result of stacking faults in the material. Introduction of anisotropic atomic displacement parameters led to only minor improvements in *R* factors. An equivalent model was used to fit the $HfMo_2O_8$ data; this sample contained no HfO_2 impurity and fewer parameters were required (113 parameters in total). The size and shape of the *hkl*-dependent peak correction for the final cycles was comparable to that derived for $ZrMo_2O_8$.

Table 1
Refinement details.

	α-$ZrMo_2O_8$	α-$HfMo_2O_8$	α'-$ZrMo_2O_8$
a (Å)	10.1416 (2)	10.10825 (9)	5.8460 (3)
c (Å)	11.7129 (3)	11.7369 (2)	5.9941 (3)
V (Å^3)	1043.29 (4)	1038.57 (2)	177.41 (2)
x_{rot}	−5.62	−5.44	0
y_{rot}	−9.15	−9.21	0
z_{rot}	−29.53	−29.69	−30
wRp (all/168/90/30/X-ray)	0.051/0.105/0.048/0.197/0.080	0.067/0.131/0.062/0.265/0.093	0.040/0.068/0.038/–/–
R_{Bragg} (168/90/30/X-ray)	0.030/0.023/0.008/0.024	0.046/0.038/0.017/0.056	0.045/0.028/–/–
Goodness-of-fit	2.72	2.36	2.47
No. of reflections (168/90/30/X-ray)	1019/379/535/14	1021/379/536/14	200/86/–/–
Structural parameters	25	25	18
Total parameters	140	113	88

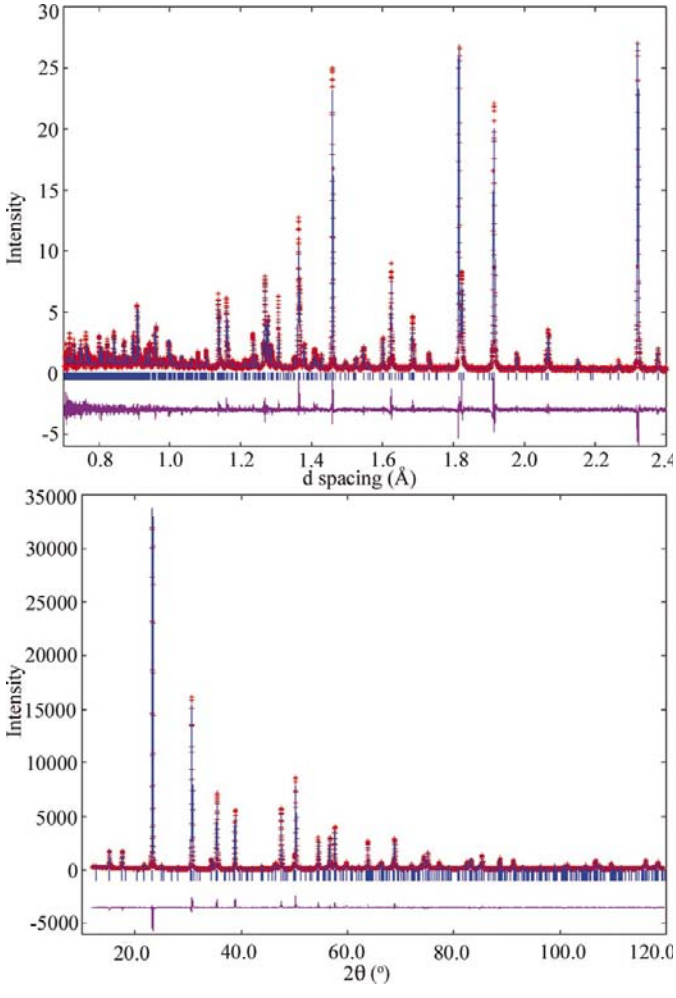

Figure 1
Final Rietveld plots for α-$HfMo_2O_8$ at room temperature. Only the 168° bank and X-ray data are shown. Observed values are shown as crosses, the calculated pattern as a solid line and the difference as the lower solid line. Predicted peak positions are marked by small vertical tick marks.

For refinements of the variable-temperature neutron data, only data from the 168° back-scattering bank was used. In these data sets, extra peaks were observed, which were due to incomplete shielding of the thermocouple and the presence of Al in the slab can walls. In an initial round of Rietveld refinements, peaks due to these materials were fitted at each temperature using the Pawley method (Pawley, 1981), as both materials were sufficiently textured that they could not be easily modelled by Rietveld refinement. Their intensities as a function of temperature were plotted and found to vary systematically and smoothly. The temperature dependence of each peak was therefore approximated by a linear function and treated as a fixed quantity in later refinements. This procedure minimizes the possibility of temperature-dependent correlations between thermocouple/can peak intensities and structural parameters, these correlations being due to the different overlap patterns caused by differing thermal-expansion coefficients. For free atomic refinements, a total of 51 parameters were refined at each temperature (12 background parameters, one scale factor, one peak-width term and one term to describe the Lorentzian character of the peak shape; 16 fractional atomic coordinates, two cell parameters and seven isotropic temperature factors for $ZrMo_2O_8$; four cell parameters; an overall temperature factor for a fixed quantity of a minor ZrO_2 impurity phase; and six parameters to describe the unit cell and peak shapes of the thermocouple/

Table 2
Selected bond distances (Å) and angles (°) for α-$ZrMo_2O_8$.

Only values of intrapolyhedral angles are listed for brevity; full details have been deposited as supplementary data.

	Zr1	Zr2	Mo			
O1		2.056 (2)	1.7798 (28)			
O2		2.095 (2)	1.7691 (22)			
O3	2.081 (2)		1.7657 (14)			
O4			1.69591 (56)			
Mo—O—Zr	172.301 (40)	156.729 (34)	161.012 (25)			
O—Zr1—O	90.530 (59)	89.470 (59)	180			
O—Zr2—O	92.299 (75)	88.29 (10)	88.621 (61)	90.785 (74)	178.89 (10)	
O—Mo1—O	108.697 (62)	109.496 (79)	106.637 (69)	110.008 (78)	111.906 (72)	109.948 (52)

Table 3
Selected bond distances (Å) and angles (°) for α-$HfMo_2O_8$.

	Hf1	Hf2	Mo	Mo—O—Hf		
O1		2.0368 (23)	1.7971 (28)	171.721 (96)		
O2		2.0623 (21)	1.7811 (31)	157.220 (30)		
O3	2.0644 (16)		1.7755 (19)	161.032 (25)		
O4			1.69355 (82)			
Mo—O—Hf	171.721 (96)	157.220 (30)	161.032 (25)			
O—Zr1—O	90.729 (62)	89.271 (62)	180			
O—Zr2—O	91.617 (68)	88.521 (96)	89.053 (56)	90.807 (73)	88.521 (96)	
O—Mo1—O	108.916 (92)	109.51 (14)	107.16 (12)	109.84 (12)	111.66 (10)	109.65 (12)

aluminium reflections). A 'rigid body' refinement model was also employed, in which the 15 fractional coordinates of atoms in the MoO_4 tetrahedron were replaced by three coordinates, three rotation angles and two internal bond distances of a 'breathing' rigid tetrahedron. Initial refinements were performed using a long room-temperature data collection. Converged refinements at a given temperature were then used to seed refinement at the next highest temperature. To avoid false minima, structural parameters were perturbed by a random amount after convergence and allowed to reconverge several hundred times at each temperature.

For refinement of the high-temperature α'-$ZrMo_2O_8$ structure, data from the neutron diffraction 168 and 90° banks were used. In the space group $P\bar{3}m1$, a total of 12 structural parameters were refined (one scale factor, two cell parameters, five fractional coordinates and four isotropic temperature factors). A further 21 parameters were used to describe the intensities and peak shapes of peaks due to the thermocouple, and 49 parameters were used to describe background, peak shapes and the ZrO_2 impurity. In the space group $P\bar{3}$, there is one additional free fractional coordinate for $ZrMo_2O_8$. For the final cycles in space group $P\bar{3}m1$, anisotropic displacement parameters were introduced, leading to a small but significant reduction in agreement factors.

Variable-temperature X-ray data were also fitted using the Rietveld method to extract thermal expansion information. For pHeniX data peaks of the Al sample plate were modelled using the Pawley method and the temperature dependence of its unit cell was used to verify temperature. For high-temperature furnace data, the Al_2O_3 internal standard was included as a second phase in the Rietveld refinement.

3. Results and discussion

3.1. Room-temperature structures

The room-temperature structures of α-$ZrMo_2O_8$ and α-$HfMo_2O_8$ were determined by combined Rietveld refinement of neutron and X-ray powder diffraction data, in which four diffraction patterns (HRPD 168, 90 and 30° bank neutron data plus laboratory X-ray data) were fitted simultaneously. The coordinates reported by Auray *et al.* (1986) were used as a starting model. There were 27 structural parameters for α-AM_2O_8 which were refined, along with the usual combination of peak shape, background and scale factors for each histogram. For $ZrMo_2O_8$, a minor ZrO_2 impurity was modelled as a second phase, with coordinates fixed at the values reported by Howard *et al.* (1988). Refinement details for both materials are included in Table 1, fractional atomic coordinates are included in the supplementary material,[1] and bond distances and angles are given in Tables 2 and 3. Rietveld plots for α-$HfMo_2O_8$ are shown in Fig. 1 .

A polyhedral representation of the structure of α-AMo_2O_8 is shown in Fig. 2. The structure can be described as containing layers of corner-sharing AO_6 octahedra and MoO_4 tetrahedra. Each octahedron shares all six of its corners with a tetrahedron, whereas each tetrahedron shares only three of its four O atoms, leaving one O atom that is formally one coordinate (referred to hereafter as $O_{terminal}$). The second nearest metal atom to this O atom lies at a distance of 3.2 Å. Individual layers are reminiscent of those in minerals such as $K_3Na(SO_4)_2$ and are separated by a van der Waals gap. The bond distances and angles (Tables 2 and 3) show that in both materials AO_6 octahedra are relatively undistorted. The $Mo—O_{terminal}$ bond is significantly shorter than the other Mo—O bonds. This feature is observed in other materials with one-coordinate O atoms and can be related to an increased π character of this bond (Auray *et al.*, 1986). Bond-valence sums are in line with those expected (Brown & Altermatt, 1985; Brese & O'Keeffe, 1991).

It is clear from Fig. 2(*b*) that the MoO_4 tetrahedra have their basal plane tilted with respect to the (001) plane, such that the $Mo—O_{terminal}$ vector is not parallel to the *c* axis. For subsequent studies as a function of temperature (*vide infra*), it is convenient to describe the tetrahedron in terms of three tilt angles relative to the crystallographic axes. Such a description has been obtained by least-squares fitting a tetrahedron with

[1] Supplementary data for this paper are available from the IUCr electronic archives (Reference: BM5004). Services for accessing these data are described at the back of the journal.

two unique bond lengths [Mo—O(—Zr) and Mo—$O_{terminal}$] to the refined coordinates. For room-temperature α-$ZrMo_2O_8$, angles of $x_{rot} = -5.62°$, $y_{rot} = -9.15°$ and $z_{rot} = -29.53°$ result. Using our angle conventions, values of 0° for x_{rot} and y_{rot} would correspond to the basal plane of the tetrahedron lying parallel to the (001) plane and the Mo—$O_{terminal}$ vector lying parallel to [001]. An angle of $z_{rot} = -30°$ results in one edge of the basal plane of the tetrahedron lying perpendicular to [100], giving rise to extra mirror planes in the structure. In other words, the interpolyhedral parallelograms visible in Fig. 2(*a*) would become rectangular for $z_{rot} = -30°$.

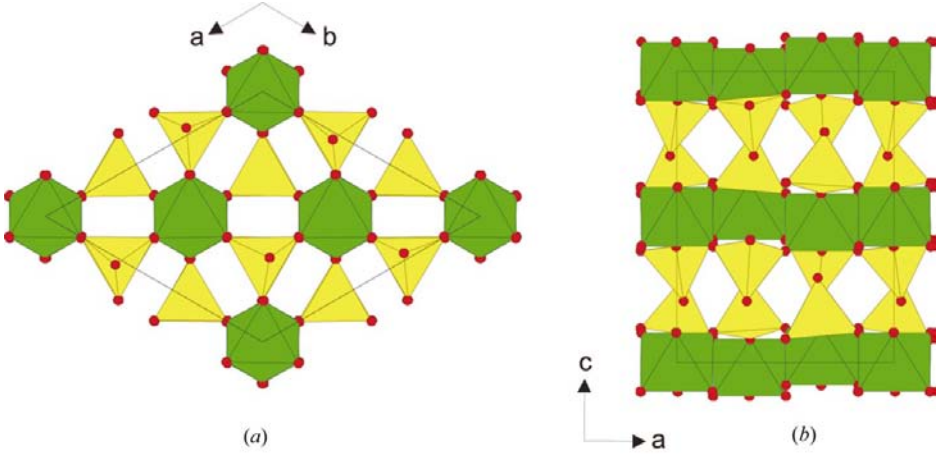

Figure 2
A polyhedral representation of the room-temperature structure of α-$HfMo_2O_8$. Layers of corner-sharing HfO_6 octahedra and MoO_4 tetrahedra stack along the *c* axis.

3.2. Thermal expansion of α-$ZrMo_2O_8$ and α-$HfMo_2O_8$

The thermal-expansion properties of α-AMo_2O_8 have been determined over a wide temperature range by powder X-ray diffraction and, for A = Zr, by powder neutron diffraction. Data were collected at 104 temperatures for $ZrMo_2O_8$ and at 136 temperatures for $HfMo_2O_8$. The unit-cell parameters derived by Rietveld refinement are shown in Fig. 3.

It is clear from Fig. 3 that the *a* cell parameter of both phases decreases over the whole temperature range, whereas the *c* parameter increases. The relative magnitude of the two opposed effects is such that the overall cell volume increases. This behaviour is unsurprising given that the van der Waals forces between layers are relatively weak and would thus be expected to give rise to facile expansion along *c*. It is also clear that the thermal expansion of both axes shows a marked discontinuity at ∼487 ($ZrMo_2O_8$) and ∼463 K ($HfMo_2O_8$). Mean coefficients of thermal expan-

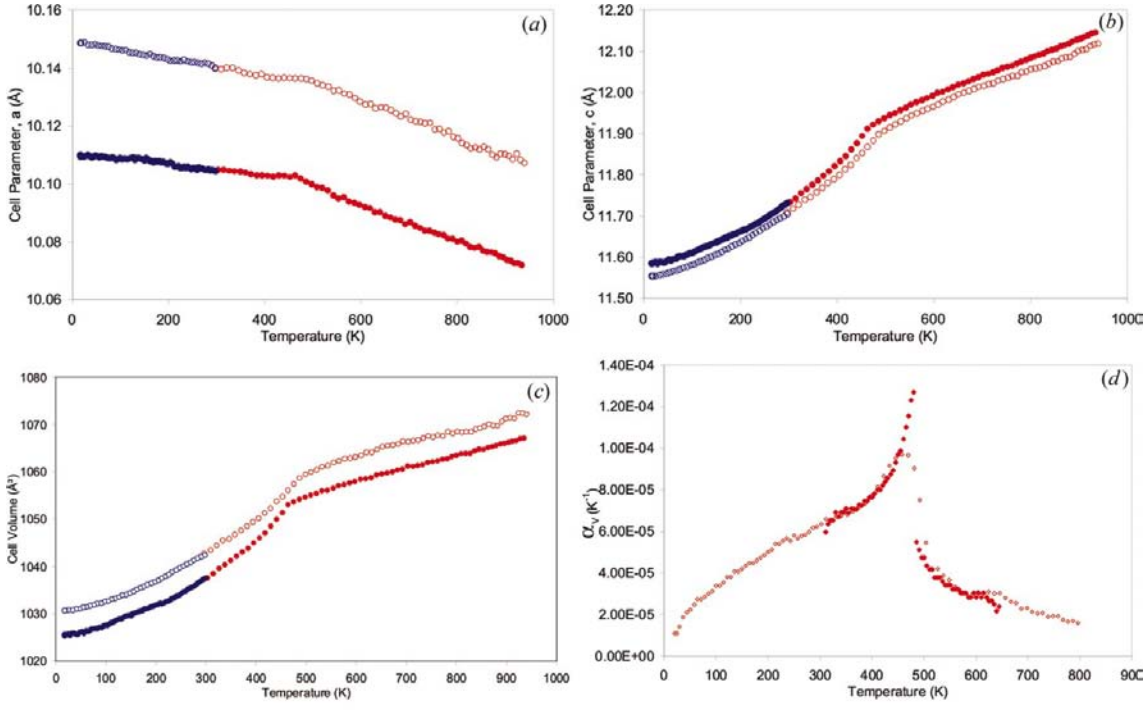

Figure 3
The temperature dependence of (*a*) *a*, (*b*) *c* and (*c*) cell volume for $ZrMo_2O_8$ (open points) and $HfMo_2O_8$ (closed points) from X-ray diffraction data. The Rietveld-derived standard uncertainties (not plotted) were 0.0004 Å, 0.0008 Å and 0.1 Å^3 for *a*, *c* and the cell volume at 300 K, and varied little with temperature. (*d*) Volume thermal expansion of $ZrMo_2O_8$ from X-ray (open points) and neutron (closed points) data.

Table 4
Thermal-expansion coefficients for $ZrMo_2O_8$ and $HfMo_2O_8$, calculated over the temperature ranges stated, using $\alpha = (V_{T2} - V_{T1})/[V_{T1}(T2 - T1)]$.

	Range (K)	α_a ($\times 10^{-6}$ K^{-1})	α_c ($\times 10^{-6}$ K^{-1})	α_V ($\times 10^{-6}$ K^{-1})
$ZrMo_2O_8$	17–440	−2.8	59.6	53.0
	520–920	−6.3	39.4	26.9
$HfMo_2O_8$	17–440	−1.7	58.7	56.6
	520–920	−6.4	39.2	26.4

sion over representative temperature ranges are shown in Table 4. Instantaneous values of α obtained from the gradient of a Bezier-smoothed function fitted to the cell-volume data of $ZrMo_2O_8$ are shown in Fig. 3(*d*). Note the good agreement in both the magnitude of α and the temperature of the discontinuity from X-ray and neutron data.

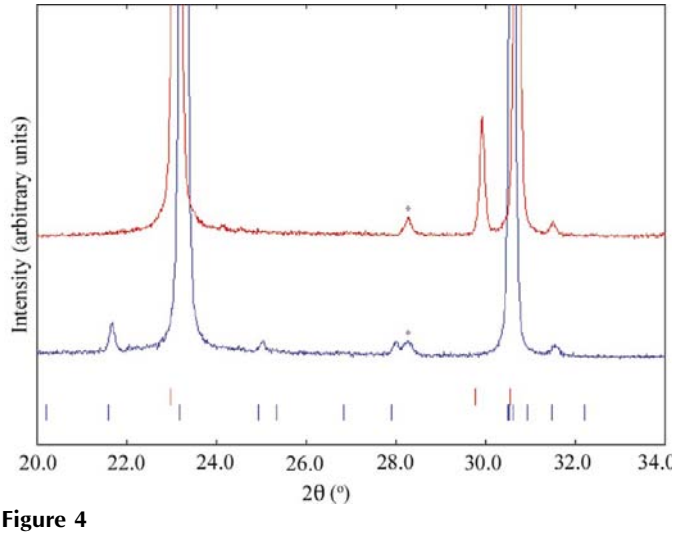

Figure 4
Diffraction data of trigonal $ZrMo_2O_8$ at 302 (lower trace) and 600 K (upper trace). Bragg reflections at ∼21.7, 25.0 and 28.0° disappear in the high-temperature pattern. The upper tick marks are for $P\bar{3}m1$ (600 K model) and the lower marks are for $P\bar{3}1c$ (302 K model). The small peaks marked with points at 28.3° are due to a minor ZrO_2 impurity. The apparent appearance of an additional peak at ∼30° 2θ at 600 K is caused by anisotropic thermal expansion that splits the (030) and (002) reflections, which have almost identical 2θ values at 302 K.

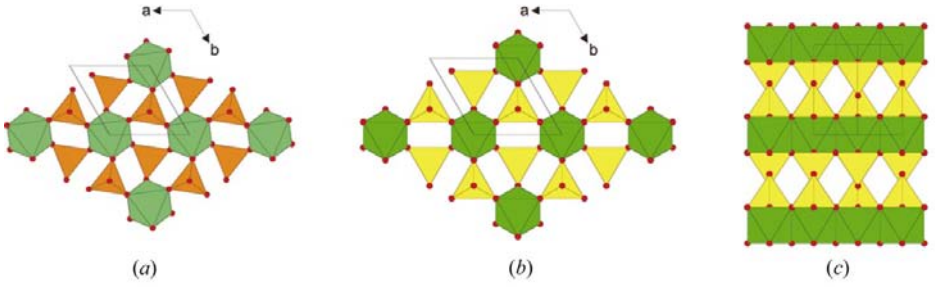

Figure 5
Structures of (*a*) $P\bar{3}$ $MnRe_2O_8$, and (*b*) and (*c*) $P\bar{3}m1$ α'-$ZrMo_2O_8$.

Table 5
Selected bond distances (Å) and angles (°) for α'-$ZrMo_2O_8$.

	Zr1	Mo	
O1	2.05183 (69)	1.78777 (65)	
O4		1.67769 (81)	
Mo—O—Zr	163.819 (16)		
O—Zr1—O	90.477 (26)	89.523 (26)	180
O—Mo1—O	108.746	110.187 (21)	

4. High-temperature structure of α'-$ZrMo_2O_8$

The observed discontinuities in cell parameters and thermal expansion for both phases at high temperature are consistent with the materials undergoing a second-order phase transition. Examination of high-temperature diffraction patterns revealed that all reflections could be indexed on a trigonal unit cell one-sixth of the volume of that at room temperature, *i.e.* with $a \simeq 5.85$ and $c \simeq 6.00$ Å. Fig. 4 compares the low- and high-temperature X-ray diffraction patterns of $ZrMo_2O_8$. The room-temperature cell is related to that at high temperature by (2 1 0; −1 1 0; 0 0 2). A similar cell has been suggested for room-temperature trigonal ZrW_2O_8 by Wilkinson *et al.* (1999) and for MRe_2O_8 (M = Mn, Co, Ni and Cu) phases by Butz *et al.* (1998). Initial attempts to fit high-temperature neutron data to a $P\bar{3}$ $MnRe_2O_8$ structure similar to that reported by Butz *et al.* (1998) led to excellent agreement between observed and calculated diffraction patterns. However, the small-volume high-temperature $P\bar{3}$ structure and the large-volume low-temperature $P\bar{3}1c$ structure are not related by a group–subgroup relationship, thus making a second-order phase transition between the structures seem unlikely. A higher-symmetry $P\bar{3}m1$ model was therefore tested. Rietveld refinement of neutron diffraction data from the 168 and 90° banks led to essentially identical wRp and R_{Bragg} factors for the two models. Atomic coordinates for O atoms in the $P\bar{3}$ refinement were also found to be within 0.06 Å of the higher-symmetry model. Given the group–subgroup relationship of $P\bar{3}1c$ and $P\bar{3}m1$, and the similar structural refinements for $P\bar{3}m1$ and $P\bar{3}$, we believe the higher-symmetry structure to be correct. As the only difference between the $P\bar{3}m1$ and $P\bar{3}$ models is the free rotation of MoO_4 tetrahedra around the threefold axis in the latter (see Fig. 5), only O-atom coordinates differ between the $P\bar{3}$ and $P\bar{3}m1$ models. Such distortions are therefore extremely difficult to determine from X-ray data alone. Refinement details for the $P\bar{3}m1$ model of α'-$ZrMo_2O_8$ are presented in Table 1, fractional coordinates are included in the supplementary material, and bond distances and angles are given in Table 5. Rietveld plots are shown in Fig. 6.

5. Variable-temperature structural studies

The high-temperature structures of the α'-AMo_2O_8 materials suggest a

displacive phase transition in which the orientation of MoO_4 tetrahedra changes continuously from low temperature as the phase transition is approached. Despite the relatively low quality of the variable-temperature neutron diffraction data (only ∼5 min of data collection per temperature), some information about the nature of the phase transition can be obtained from them. Initially, MoO_4 groups were treated as rigid tetrahedra [although the Mo—O(—Zr) and $Mo—O_{terminal}$ distances within tetrahedra were allowed to refine freely] and each of the 72 neutron data sets recorded between 300 and 647 K was refined using the low-temperature $P\bar{3}1c$ structural model. The same analysis was then repeated, with tetrahedra constrained to have x_{rot} and y_{rot} values of 0° [*i.e.* to have their tetrahedral basal plane parallel to (001), as in the high-temperature structure]. In Fig. 7(*a*) we plot the difference in *wRp* values obtained at each temperature [*wRp*(free) − *wRp*(constrained)]. The *R*-factor discrepancy falls to a low (essentially zero) value at the same temperature as the discrepancy in unit-cell parameters, showing that the rapid data collections do contain significant structural information about tetrahedral orientations and support the $P\bar{3}m1$ structural model at high temperature. Analysis of the 300 K data set shows that moving refined tetrahedral angles from their ideal values by 2σ (where σ is the Rietveld-derived standard uncertainty in the angle) leads to an *wRp* increase of ∼0.08%. We can therefore assign a profile *R*-factor discrepancy of greater than 0.08% in Fig. 7 as representing a reasonable confidence level that two tetrahedral orientations are inequivalent. Alternatively, we can say that when *wRp*(free) − *wRp*(ideal) is less than 0.08%, the diffraction data contain no significant information about non-zero tetrahedral tilt angles.

Fig. 8 contains key parameters derived from the variable-temperature refinements. Fig. 8(*a*) shows the temperature dependence of the tetrahedral tilt angles, x_{rot} and y_{rot}. These approach 0° in a smooth fashion as the temperature approaches T_C. Equivalent plots are obtained by free atomic refinement followed by fitting a rigid tetrahedron to the refined coordinates. The *x* and *y* coordinates of the centre of the MoO_4 tetrahedron approach $x = y = 1/3$ as T_C is approached (Fig. 8*b*). Both these observations provide further support for the low-to-high symmetry displacive phase transition. The

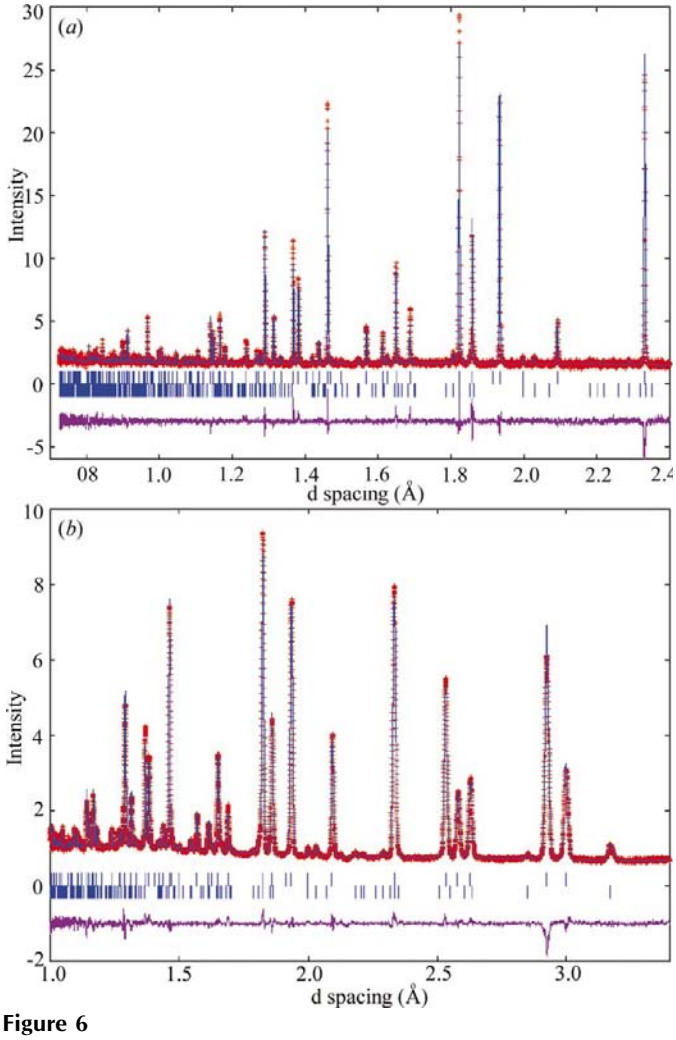

Figure 6
Rietveld refinements of the (*a*) 168° and (*b*) 90° banks for α'-$ZrMo_2O_8$ at 647 K. The upper tick marks show α'-$ZrMo_2O_8$ peak positions and the lower tick marks show peaks due to a minor ZrO_2 impurity.

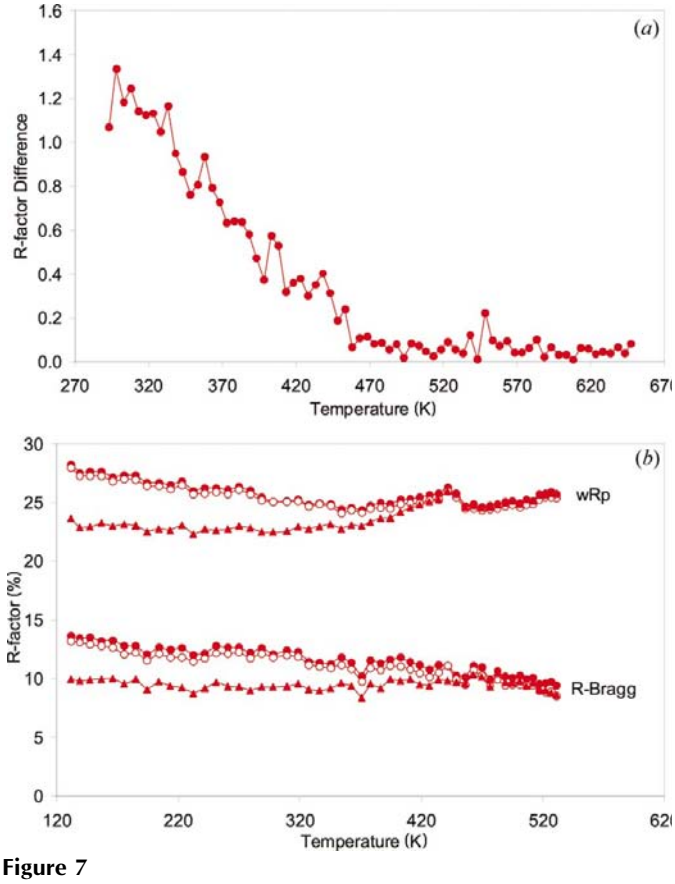

Figure 7
(*a*) The *R*-factor discrepancy for neutron diffraction refinements of a tetrahedron constrained to have $x_{rot} = y_{rot} = 0°$ *versus* free refinement. (*b*) The *wRp* and Bragg *R* factors for variable-temperature X-ray refinements of $HfMo_2O_8$. Closed triangles represent parameters from the $P\bar{3}1c$ refinement, open circles the $P\bar{3}$ refinement and closed circles the $P\bar{3}m1$ refinement. Above T_C, refinements for all models give equivalent *R* factors.

apparent average Mo—O(—Zr) distance remains essentially unchanged as a function of temperature ($d = 1.795 + 5.9 \times 10^{-6}\,T$ Å), whereas a small contraction ($d = 1.680 - 5.7 \times 10^{-5}\,T$ Å) was observed for the Mo—$O_{terminal}$ bond. These observations are presumably related to motions of the MoO_4 group, which lead to an increasing underestimation of the true bond length as motions increase (Busing & Levy, 1964); higher motion of Mo—$O_{terminal}$ (as evidenced by its atomic displacement parameters) is sufficient that an apparent bond contraction is observed. The mean Zr—O bond distances ($d = 2.068 - 7.8 \times 10^{-6}\,T$ Å) remain essentially unchanged over the temperature range studied, again suggesting that minor increases in the true Zr—O distance are offset by artificial shortening caused by correlated motion.

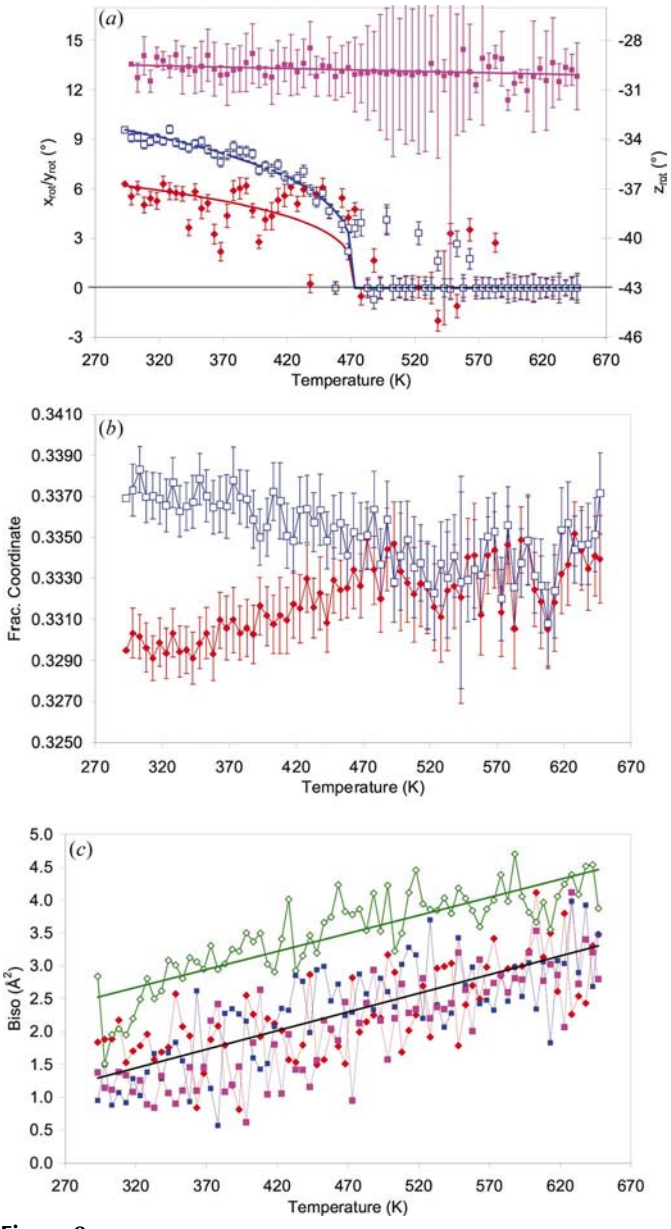

Figure 8
(*a*) Tetrahedral rotation angles x_{rot} (closed diamonds), y_{rot} (open squares) and z_{rot} (closed squares, right-hand scale) as a function of temperature. In the high-temperature phase, x_{rot} and y_{rot} are ill-defined. Values from refinements in which wRp(free) − wRp(ideal) < 0.08% (see text), which contain no significant information about non-zero tilt angles, are therefore plotted as 0. (*b*) *x*/*y* fractional atomic coordinates of the tetrahedron centre as a function of temperature. (*c*) Isotropic temperature factors of atoms O1, O2, O3 (closed points) and O4 (open points) as a function of temperature. No significant discontinuities are observed at T_C.

This model for the phase transition allows some speculation as to the origins of the relative changes in magnitude of α_a and α_c at the phase transition. Below T_C, trends in x_{rot}/y_{rot} of the MoO_4 tetrahedron show that thermal vibrations lead to the Mo—$O_{terminal}$ vector becoming more closely aligned with the *c* axis. This process can only occur as the interplanar separation increases and the MoO_4 tetrahedra of adjacent layers become less interdigitated. Above T_C, where the Mo—$O_{terminal}$ vector is, at least on average, parallel to the *c* axis, there is no such contribution to the thermal expansion along *c*, and the value of α_c decreases. The contraction of the *a* axis over the entire temperature range can presumably be ascribed to the population of negative Gruneisen parameter modes involving the coupled rotations of rigid or quasi-rigid tetrahedra and octahedra. Such RUMS (rigid unit modes) or quasi-RUMs are responsible for isotropic negative thermal expansion in α-ZrW_2O_8 and a number of other framework materials (Pryde *et al.*, 1996, 1997). The increased contraction above T_C implies the increased amplitude of such motions in the α' phase.

Variable-temperature neutron data for α-$HfMo_2O_8$ that would provide conclusive evidence as to its high-temperature structure have not been obtained to date. Variable-temperature X-ray data suggest that its high-temperature structure is isostructural to that of α'-$ZrMo_2O_8$. Fig. 7(*b*) shows *R* factors obtained by Rietveld refinement of X-ray data recorded between 100 and 533 K using the three different structural models discussed for $ZrMo_2O_8$. Below ∼460 K, the *R* factor for the $P\bar{3}1c$ model is significantly better than that using either the $P\bar{3}$ or the $P\bar{3}m1$ models. Above this temperature, essentially identical *R* factors can be obtained with each model. It therefore seems reasonable to conclude that α'-$HfMo_2O_8$ also has the simple $P\bar{3}m1$ structure at high temperature.

6. Conclusion

Trigonal $ZrMo_2O_8$ and $HfMo_2O_8$ have been shown to undergo a displacive phase transition from their low-temperature $P\bar{3}1c$ α form to a high-temperature $P\bar{3}m1$ α' form. The thermal expansion of the two phases differs considerably, being much lower for the high-temperature phase. The structure of the high-temperature form has been determined by neutron powder diffraction and a mechanism for the phase transition has been described.

The authors would like to thank the EPSRC for financial support under grant No. GR/N00524, for provision of X-ray diffraction equipment under grant No. GR/M35222 and for access to neutron diffraction facilities. The authors would also like to thank Dr Richard Ibberson of the Rutherford Appleton Laboratory for assistance during data collections,

and the ISIS support staff for the provision and maintenance of sample environment apparatus.

References

Achary, S. N., Mukherjee, G. D., Tyagi, A. K. & Godwal, B. K. (2002). *Phys. Rev. B*, **66**, 184106.

Achary, S. N., Mukherjee, G. D., Tyagi, A. K. & Godwal, B. K. (2003). *Powder Diffr.* **18**, 147–149.

Allen, S. & Evans, J. S. O. (2003). *Phys. Rev. B*, **68**, 134101.

Allen, S. & Evans, J. S. O. (2004). Accepted for publication (DOI: 10.1039/6310137a).

Allen, S., Warmingham, N. R., Gover, R. K. B. & Evans, J. S. O. (2003). *Chem. Mater.* **15**, 3406–3410.

Auray, M., Quarton, M. & Tarte, P. (1986). *Acta Cryst.* C**42**, 257–259.

Auray, M., Quarton, M. & Tarte, P. (1987). *Powder Diffr.*, **2**, 36–38.

Brese, N. E. & O'Keeffe, M. (1991). *Acta Cryst.* B**47**, 192–197.

Brown, I. D. & Altermatt, D. (1985). *Acta Cryst.* B**41**, 244–247.

Bruker (2000). *TOPAS*. Version 2.0. Bruker AXS Ltd, Karlsruhe, Germany.

Busing, W. R. & Levy, H. A. (1964). *Acta Cryst.* **17**, 142–146.

Butz, A., Miehe, G., Paulus, H., Strauss, P. & Fuess, H. (1998). *J. Solid State Chem.* **138**, 232–237.

Carlson, S. & Krogh Andersen, A. M. (2000). *Phys. Rev. B*, **61**, 11209–11212.

Evans, J. S. O. (1999). *J. Chem. Soc. Dalton Trans.* pp. 3317–3326.

Evans, J. S. O., Hanson, P. A., Ibberson, R. M., Kameswari, U., Duan, N. & Sleight, A. W. (2000). *J. Am. Chem. Soc.* **122**, 8694–8699.

Evans, J. S. O., Hu, Z., Jorgensen, J. D., Argyriou, D. N., Short, S. & Sleight, A. W. (1997). *Science*, **275**, 61–65.

Freundlich, W. & Thoret, J. (1967). *C. R. Acad. Sci. Ser. C*, **265**, 96–98.

Grzechnik, A., Crichton, W. A., Syassen, K., Adler, P. & Mezouar, M. (2001). *Chem. Mater.* **13**, 4255–4259.

Howard, C., Hill, R. & Reichert, B. (1988). *Acta Cryst.* B**44**, 116–120.

Klevtsova, R. F., Glinskaya, L. A., Zolotova, E. S. & Klevtsov, P. V. (1989). *Dokl. Akad. Nauk SSSR*, **305**, 91–95.

Krogh Andersen, A. M. & Carlson, S. (2001). *Acta Cryst.* B**57**, 20–26.

Lind, C., VanDerveer, D. G., Wilkinson, A. P., Chen, J. H., Vaughan, M. T. & Weidner, D. J. (2001). *Chem. Mater.* **13**, 487–490.

Lind, C., Wilkinson, A. P., Rawn, C. J. & Payzant, E. A. (2002). *J. Mater. Chem.* **12**, 990–994.

Mary, T. A., Evans, J. S. O., Vogt, T. & Sleight, A. W. (1996). *Science*, **272**, 90–92.

Mittal, R., Chaplot, S. L., Lalla, N. P. & Mishra, R. K. (1999). *J. Appl. Cryst.* **32**, 1010–1011.

Muthu, D. V. S., Chen, B., Wrobel, J. M., Andersen, A. M. K., Carlson, S. & Kruger, M. B. (2002). *Phys. Rev. B*, **65**, 064101.

Pawley, G. S. (1981). *J. Appl. Cryst.* **14**, 357–361.

Pryde, A. K. A., Hammonds, K. D., Dove, M. T., Heine, V., Gale, J. D. & Warren, M. C. (1996). *J. Phys. C*, **8**, 10973–10982.

Pryde, A. K. A., Hammonds, K. D., Dove, M. T., Heine, V., Gale, J. D. & Warren, M. C. (1997). *Phase Transit.*, **61**, 141–153.

Rimsky, A., Thoret, J. & Freundlich, W. (1968). *C. R. Acad. Sci. Ser. C*, **267**, 1468–1470.

Samant, M. S., Dharwadkar, S. R., Phadnis, A. B. & Namboodiri, P. N. (1993). *Mater. Chem. Phys.* **35**, 120–125.

Taylor, D. (1984). *Br. Ceram. Trans. J.* **83**, 92–98.

Thoret, J. (1974). *Rev. Chim. Miner.* **11**, 237–261.

Trunov, V. K. & Kovba, L. M. (1967). *Russ. J. Inorg. Chem.* **12**, 1703–1704.

Wang, K. & Reeber, R. R. (2000). *Philos. Mag. A*, **80**, 1629–1643.

Wilkinson, A. P., Lind, C. & Pattanaik, S. (1999). *Chem. Mater.* **11**, 101–108.